PERGAMON

International Journal of Heat and Mass Transfer 44 (2001) 1593–1603

International Journal of HEAT and MASS TRANSFER

www.elsevier.com/locate/ijhmt

Heat transfer studies of a porous heat sink characterized by straight circular ducts

H.Y. Zhang, X.Y. Huang *

School of Mechanical and Production Engineering, Nanyang Technological University, Nanyang Avenue, Singapore 639798, Singapore

Received 28 January 2000; received in revised form 22 May 2000

Abstract

This paper aims to investigate both experimentally and analytically the heat transfer characteristics in a porous heat sink characterized by straight circular ducts. This kind of heat sink is appreciated in miniaturized heat dissipation applications owing to the low flow resistance in comparison with its bead-characterized counterparts. The test systems were established for air and water flows and the experiments were conducted with the cell Reynolds number *Re* ranging from 6.7 to 545 and 8.5 to 990, respectively. The theoretical modeling is conducted based on a two-equation model. The measured wall temperature rises and the Nusselt numbers are presented for both working fluids. In the air experiment, a $Re^{1.05}$ dependence is found for the Nusselt number, while in the water experiment, the *Re* dependence is logarithmic. The theoretical results are compared with the experimental measurements and the agreement is satisfactory.

1. Introduction

With the trend towards increasing scales of integration in the IC industry, heat sinking technologies with higher level of performance are required to pursue and develop to meet the elevated power dissipation requirement in electronic devices. To this end, the microchannel structure has been proposed as a high-effective cooling technique and the corresponding experiment and analysis showed that the heat removal capacity approached as much as 790 W/cm^2 or even more [1,2]. More detailed analysis of the heat transfer in microchannels can be found in recent literature such as the numerical study by Yin and Bau [3].

The use of porous media is another effective means in the heat removal from electronic components. Testing and modeling of porous systems under lateral wall heating condition have been conducted for various porous structures [4–12] and, mostly, porous systems characterized by spherical beads were used. Although the heat transfer results may vary from case to case [6], conclusion has been drawn that the heat transfer capacity in porous systems increases as the representative pore size decreases, which is known as the miniaturization in the cooling technologies. On the other hand, however, a decrease in pore size leads to a much increased pressure drop or flow resistance due to the flow tortuosity inherent in most porous systems, which becomes difficult to maintain in miniaturized heat sink units.

To overcome this shortcoming, practices with the use of porous systems characterized by straight ducts are recommended on the guiding principle that a less tortuous pore structure will produce a lower flow resistance. As we will demonstrate in this paper, the flow resistance for porous heat sinks characterized by straight circular ducts is generally 10 times less than that for bead-characterized counterparts whereas the overall heat transfer is not weakened. Thus, in the efforts to seek more cost-effective heat dissipation units, straight-duct characterized porous heat sinks are much appreciated and require intensive studies in both theory and experiment. Based on the volume averaging method [13,14], Zhang et al. [15] conducted a two-equation modeling for porous media characterized by straight rectangular ducts. It was found that the Nusselt number based on

* Corresponding author. Tel.: +65-790-4448.
E-mail address: mxhuang@ntu.edu.sg (X.Y. Huang).

0017-9310/01/$ - see front matter
PII: S0017-9310(00)00194-0

Nomenclature

A	$=WH$, apparent flow cross-section area
A_l	$=H/l$, the ratio of the system height to the unit cell length scale
A_L	$=L/H$, the length to height ratio
c_0	empirical constant
$c_{f,app}$	apparent friction factor for in-tube flow
d_c	diameter of a circular tube
d_p	bead diameter
$f(x)$	correction function, Eq. (9)
G	volumetric flowrate
h	heat transfer coefficient, Eq. (3)
H	height
H_{uc}	unit-cell-level heat transfer coefficient
k_f, k_s	thermal conductivity of the fluid and the solid, respectively
$K_{f,eff}$, $K_{s,eff}$	effective thermal conductivities in energy Eqs. (5), (6), reduced by k_f
$K_{fs,zz}$, $K_{sf,zz}$	thermal conductivity components in the volume averaging method
l	length scale of a unit cell, $=d_p$ for a bead-characterized porous system
L	length of a porous system
Nu	Nusselt number, Eq. (4)
Pr	Prandtl number
Q_{net}	net heat input rate
Q_f	thermal energy rate transported by the fluid
Q_t	electrical heating power input
Re	$=\rho Gl/\mu A$, cell Reynolds number
T	temperature
T_1, T_2, T_3	wall temperatures at locations $L/6$, $L/2$ and $5L/6$ from the inlet, respectively
u_m	$=G/A$, mean velocity
W	width
x, z	dimensionless coordinate variables in longitudinal and transverse directions, respectively, reduced by H

Greek symbols

ε	volume fraction for the fluid
γ	permeability for sintered bead systems
κ	solid-to-fluid thermal conductivity ratio
μ	dynamic viscosity for the fluid dimensionless temperature
ρc	heat capacity for the fluid
τ	flow resistance

Subscripts

f	fluid
in	inlet fluid
m	mean
s	solid
w	heated wall

the wall to the bulk fluid temperature difference was mainly determined by the solid-to-fluid conductivity ratio and varied with the product of the cell Reynolds number and Prandtl number, or the cell Peclet number. This modeling was limited to the fluid flow with a low or moderate cell Peclet number. With a modification in the solid–fluid heat transfer coefficient at the unit cell level, the volume averaging model was extended to laminar fluid flow cases with a high Peclet number [16]. Experimental investigation of the heat transfer in porous systems characterized by straight ducts was not reported. An overall assessment of such type of porous systems as against other types of porous systems was not conducted as well.

In this paper, we deal both experimentally and analytically with the heat transfer problem in a porous heat sink characterized by straight circular ducts, as illustrated in Fig. 1. Heat is input from the upper sidewall of the heat sink and then transported by the working fluid. In contrast to the random pore structure and tortuous flow in most porous systems, the straight circular ducts are uniformly and unidirectionally arranged in a solid matrix so that the working fluid flows through at the shortest path. The test systems were established for two easily available working fluids, air and water. The theoretical analysis associated with the two fluids is performed based on the

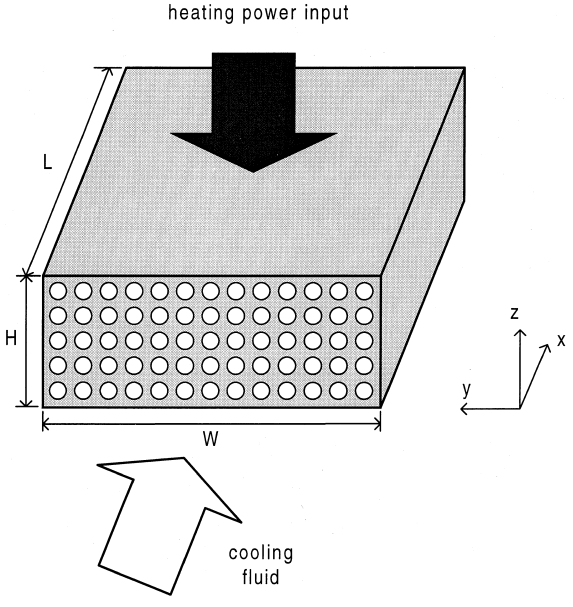

Fig. 1. A porous heat sink characterized by straight circular ducts with heat being input from the upper wall.

previous modified model [16]. Moreover, the heat transfer results from straight-duct characterized porous heat sinks are compared with the reported results from the bead-characterized counterparts. It is found that the porous heat sink investigated in this paper is capable of providing an equivalent heat transfer capacity with a greatly reduced flow resistance, and that the heat transfer can be even better when the flow resistance in the two cases is maintained at the same level.

2. Experimental measurement

2.1. Test systems

The test system for air flow is schematically shown in Fig. 2. The pressure head was produced by an air compressor with an adjustable supply pressure ranging from 0 to 100 psi. The flowrate was measured by air flowmeters with a factory-calibrated accuracy of 2.5% in full scale but different measurement ranges. In the experiment, only the flowrate above 25% of the full scale was recorded to ensure sufficient accuracy. The flowrate was fine tuned by the needle valve. A filter was connected in the airway upstream the flowmeters. For the water experiment, the pressure head was maintained by the tap water and the flowrate was obtained by measuring the volume of water during a time interval. All the water experiments were conducted at late night times to minimize the fluctuation in the pressure head and flow rate. The working fluid, air or water, was forced through the test section, carrying away the heat input from the upper sidewall of the porous heat sink.

The detail of the test section is shown in Fig. 3. It mainly consists of the porous heat sink, the strip heater and the temperature measurement apparatus. The porous heat sink, fabricated by uniformly drilling 5×13 circular ducts in a rectangular aluminum alloy block (see Fig. 1), is 60 mm long (L), 31.2 mm wide (W) and 12 mm high (H), with a machining excess of 0.4 mm. The diameter d_c of each duct is 1.5 mm. The porous heat sink was connected mechanically to the flow channels with flanges and adapter sleeves. The flow channels upstream and downstream the test section were made of PVC, with the inner diameters 25 and 14 mm, respectively. The slenderer inner diameter for the downstream flow channel helped to improve the measurement of the mixed mean fluid temperature at the outlet of the test section.

The strip heater was attached on the upper surface of the heat sink, simulating the heating from an electronic component. The heating power input Q_t was read out from a digital voltmeter in parallel connection and a digital ammeter in series connection, and could be varied by adjusting an a.c. variac. An aluminum foil tape was used between the heater and the upper wall to ensure good thermal contact. The heat sink was thermally insulated from the ambient environment.

To implement the temperature measurements of the heated wall, three pairs of slots with rectangular cross-sections of 1.5×0.6 mm^2 were milled in the upper wall of the heat sink, 10, 30 and 50 mm downstream the inlet of the heat sink, respectively. Three pairs of thermocouples were installed inside the corresponding slot pairs, with each pair of thermocouples measuring the wall temperatures right at the centerline and 10 mm off the centerline. Each thermocouple was fixed with a fine copper mesh sheet to ensure good thermal contact with the wall. The detailed arrangement of the thermocouples is shown in Fig. 3. The arithmetic averages of the measured temperature pairs at the same longitudinal locations are denoted by T_1, T_2 and T_3 representing the wall temperature profiles, respectively. The effect of the slots on the overall heat transfer was negligible while the accommodation of thermocouples in the slots avoided

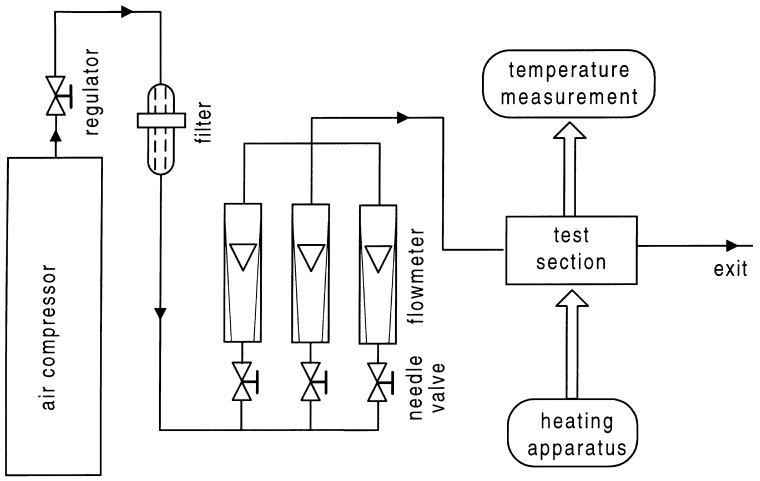

Fig. 2. Schematic of the air-cooling system.

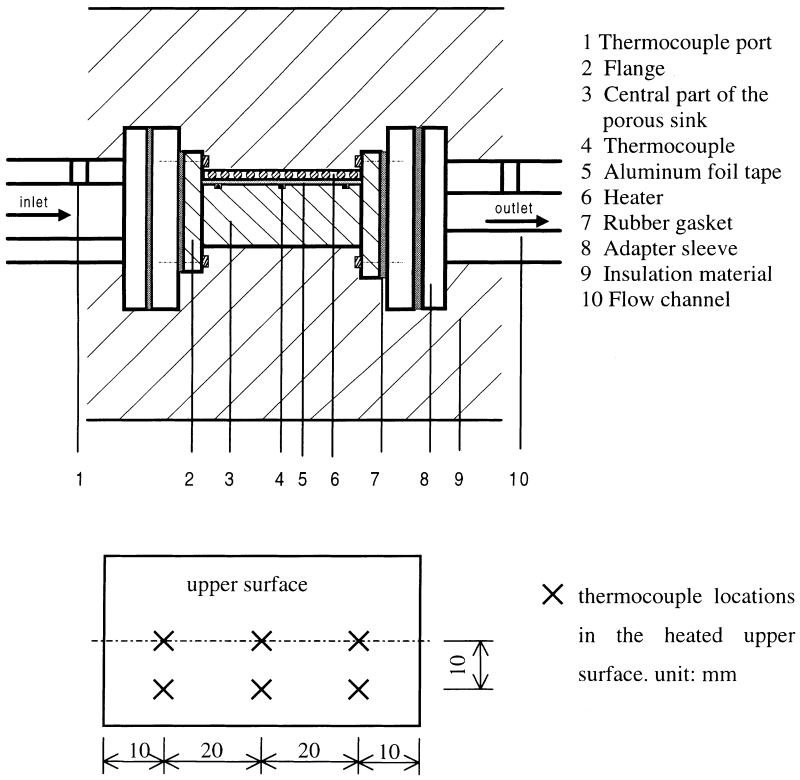

Fig. 3. The test section.

direct contacting of the thermocouples heads with the heater and thus warranted more accurate measurements.

Two thermocouples were deployed in the flow channels 40 mm upstream the inlet and 80 mm downstream the outlet of the heat sink to measure mixed mean fluid temperatures at the inlet and outlet. The locations of the two thermocouples could be altered in the cross-sections to examine the temperature variation in the flow cross-section. Two calibrated digital thermometers were used for temperature reading.

2.2. Experimental procedure

For air flow, the test was conducted under the following conditions: the heating power input Q_t was varied from 8 to 30 W, the flowrate G was from 1 to 81 l/min and the cell Reynolds number Re, defined by $\rho Gl/\mu A$, was from 6.7 to 545. For the water experiment, Q_t was varied from 40 to 130 W, G from 1.13 to 132 ml/s and Re from 8.5 to 990. The experiment was started by forcing the working fluid through the test system and then switching on the electrical heater. After a certain time period, typically 2 h for the air experiment and 30 min for the water experiment, the thermal equilibrium was achieved, at which the variation in the wall temperature was observed less than 0.1°C in several minutes. The wall temperatures and the fluid temperatures at the inlet and outlet, as well as the flowrate, were recorded simultaneously.

The net thermal energy rate transported by the fluid was determined by two ways, depending on the flowrate. At a flowrate larger than a reference flowrate G_0 ($G_0 = 30$ l/min for air flow and 6 ml/s for water flow), we first found the heat loss by inputting an electrical heating power to the test section under no-flow condition and, when the thermal equilibrium was attained, this power input was taken as the heat loss Q_{loss}. In the experiment, a heat loss of 3.9 W was found at a mean wall temperature of 60°C. Under normal test conditions, the net thermal energy was obtained by the power input minus the heat loss, i.e.,

$$Q_{net} = Q_t - Q_{loss}, \quad G > G_0. \tag{1}$$

As for the low flowrate case, the heat loss became comparable in magnitude to Q_t and Eq. (1) would lead to a significant error in Q_{net}. Since in this situation the outlet fluid temperature was relatively uniform in the cross-section, the net thermal energy carried away by the fluid can be calculated by the inlet to outlet fluid temperature difference, ΔT_f, i.e.,

$$Q_{net} = \rho c u_m A \Delta T_f = \rho c G \Delta T_f, \quad G \leqslant G_0. \tag{2}$$

The heat transfer coefficient, h, for the porous heat sink is obtained by

$$h = \frac{Q_{\text{net}}}{LW(T_{\text{w,m}} - T_{\text{in}})}, \tag{3}$$

where $T_{\text{w,m}}$ is the mean of T_1, T_2 and T_3. The overall Nusselt number is calculated by

$$Nu = \frac{hH}{k_{\text{f}}}, \tag{4}$$

L, W and H in Eqs. (3) and (4) are the length, width and height of the porous heat sink illustrated in Fig. 1. Note that, in this experimental procedure, all the material properties were based on the inlet fluid temperature.

2.3. Measurement uncertainty

Type-T thermocouples (copper–constantan) were utilized to measure both the fluid and the wall temperatures. These thermocouples were carefully made so that the indicated temperatures in the thermometers deviated within 0.2°C with a temperature calibrator at 25°C and 70°C. Thermocouples with a deviation larger than 0.2°C were disused. Thus the errors in temperature measurements with thermocouples were estimated to be 0.2°C. The maximum error in the volumetric flow rate G and the cell Reynolds number Re was estimated to be 8%. The error of the input electrical power Q_{t} was about 2%, while the error of Q_{net} at small flowrates was less than 7%. With Eqs. (1)–(4) and the root-sum square method [17], we estimated that the uncertainty of h and Nu was 10% for the air experiment and varied from 7% to 13% for the water experiment, depending on the flow conditions.

3. Theoretical analysis

In the theoretical analysis, the fluid and the solid are treated as continua. Considering the uniform and straight microstructure characterized in the present test model, macroscopically the Darcy flow is imposed, while at the unit cell level the laminar flow is assumed. The transverse thermal dispersion which is generally used in describing heat transfer in bead-characterized porous systems vanishes here due to the unidirectional flow in straight ducts. The material properties are assumed constant, evaluated at the inlet fluid temperature. The x-direction heat transfer of the solid matrix at the inlet and the outlet to the fluid is ignored. Since in the experiments the lateral walls of the heat sink were insulated, the spanwise heat transfer is not considered and the problem is two-dimensional. The dimensionless energy equations for the fluid and the solid are written as

$$\varepsilon\frac{\partial^2\theta_{\text{f}}}{\partial x^2} + K_{\text{f,eff}}\frac{\partial^2\theta_{\text{f}}}{\partial z^2} + A_l^2 H_{\text{uc}} f(x)(\theta_{\text{s}} - \theta_{\text{f}}) = A_l Re\, Pr\frac{\partial\theta_{\text{f}}}{\partial x}, \tag{5}$$

$$(1-\varepsilon)\kappa\frac{\partial^2\theta_{\text{s}}}{\partial x^2} + K_{\text{s,eff}}\frac{\partial^2\theta_{\text{s}}}{\partial z^2} - A_l^2 H_{\text{uc}} f(x)(\theta_{\text{s}} - \theta_{\text{f}}) = 0, \tag{6}$$

where θ_{f} and θ_{s} are the dimensionless temperatures for the fluid and the solid, defined by

$$\theta_{\text{f}} = \frac{T_{\text{f}} - T_{\text{in}}}{T_{\text{w,m}} - T_{\text{in}}}, \tag{7}$$

$$\theta_{\text{s}} = \frac{T_{\text{s}} - T_{\text{in}}}{T_{\text{w,m}} - T_{\text{in}}}, \tag{8}$$

ε is the volume fraction of the fluid, κ is the solid-to-fluid thermal conductivity ratio, and $Re\,Pr$ is the product of Re and Pr. It should be pointed out that θ_{f} and θ_{s} do not denote the actual point-wise temperature fields in porous media. Rather, they represent the volume averaged temperature fields and are meaningful at the macroscopic level.

The feature of the energy Eqs. (5) and (6) lies in the fact that the effects of the microstructure and the constituents' properties are incorporated into the transport parameters. These transport coefficients are obtainable using the volume averaging analysis [13–16]. The effective thermal conductivities in the x direction are obtained immediately as the intrinsic values for the two phases. $K_{\text{f,eff}}$ and $K_{\text{s,eff}}$ represent the effective thermal conductivities in the z direction and can be numerically determined following the numerical method in [15]. Different from [15,16], the additional conductivity components in the volume averaging analysis, i.e., $K_{\text{fs,zz}}$ and $K_{\text{sf,zz}}$ (see [16]) are combined in the conventional conductivities so as to be consistent with most empirical models. Such a combination does not produce a significant deviation (less than 1%) from the modeling equations given in [16]. The sum of $K_{\text{f,eff}}$ and $K_{\text{s,eff}}$ corresponds to the effective thermal conductivity in the one-equation modeling. For the air flow case, $\kappa = 4580$ and we find that $K_{\text{f,eff}} = 0.476$ and $K_{\text{s,eff}} = 2400$. For the water flow case, where $\kappa = 200$, much smaller than the air flow case, we obtain $K_{\text{f,eff}} = 0.475$ and $K_{\text{s,eff}} = 105.1$. It is the discrepancy in κ that renders $K_{\text{s,eff}}$ significantly different for the two cases and, as will be shown later, affects the heat transfer patterns in connection with Re.

The solid-to-fluid heat transfer coefficient in the last terms on the left-hand side of the energy equations (5) and (6) consist of three parameters: the macroscopic to microscopic length scale ratio $A_l = H/l$, the unit-cell-level heat transfer coefficient H_{uc}, and a correction function $f(x)$. A_l is not related to the detail of the unit cell geometry and the constituents. For a given H, the smaller the cell length scale l is, the higher A_l and the

overall heat transfer rate are. In the present case, $l = 2.4$ mm and $A_l = 5$. The determination of H_{uc} requires a closure solution over a unit cell as discussed in [13,14] and [16]. In our cases, it is found that $H_{uc} = 25.13$ for air flow and 25.08 for water flow. In fact, the value of H_{uc} becomes very close to the asymptotic result 8π at $\kappa > 100$. The function $f(x)$ used in Eqs. (5) and (6) accounts for the thermal entrance effect on the heat transfer coefficient at the unit cell level, which has been justified in detail in [16]. It is determined by

$$f(x) = \frac{c_0 Nu_x}{Nu_x|_{x\to\infty}}. \tag{9}$$

Here Nu_x, the local Nusselt number for a circular tube with a diameter d_c under the isothermal boundary condition, can be found in [18] and has its asymptotic value $Nu_x|_{x\to\infty} = 3.657$ when the heat transfer is fully developed. The empirical coefficient c_0 was numerically found to be around 0.5 for porous systems characterized by straight rectangular ducts with $\kappa = 10^3$ [16]. In the present analysis, although the geometry of the straight duct is circular and the values of κ are different, the value of 0.5 for c_0 is still used. As will be shown later, the theoretical analysis with this value for c_0 agrees well with the experiment.

The boundary conditions for the energy equations (5) and (6) are given as follows:

$$\theta_f = 0, \quad \frac{\partial\theta_s}{\partial x} = 0, \quad \text{at } x = 0, \tag{10}$$

$$\frac{\partial\theta_f}{\partial x} = \frac{\partial\theta_s}{\partial x} = 0, \quad \text{at } x = A_L, \tag{11}$$

$$\frac{\partial\theta_f}{\partial z} = \frac{\partial\theta_s}{\partial z} = 0, \quad \text{at } z = 0, \tag{12}$$

$$\theta_f = \theta_s = \theta_w(x), \quad \text{at } z = 1. \tag{13}$$

Note that the wall temperature $\theta_w(x)$ in Eq. (13) can be found from the experimental measurement. For an isothermal wall,

$$\theta_f = \theta_s = \theta_w(x) \equiv 1, \quad \text{at } z = 1. \tag{14}$$

By using Eqs. (2) and (4), the Nusselt number takes the form

$$Nu = \frac{A_l}{A_L}\frac{RePr}{\theta_{w,m}}\int_0^1 \theta_f|_{x=A_L}\mathrm{d}z. \tag{15}$$

The energy Eqs. (5) and (6) are discretized by the control-volume finite difference method and solved by the Tri-Diagonal Matrix Algorithm (TDMA). The detail has been discussed in [19] and is not shown here. The numerical solution is viewed to be convergent when the relative changes between successive iterations in a monitoring temperature and the Nusselt number are less than 10^{-6}. A grid system with a size of 46×62 is employed and finer grid steps are deployed in the regions near the boundaries of the entrance and the heated wall. The Nusselt numbers from this grid size are compared with those from a finer grid size of 66×92 at two values of $RePr$: 30 and 300. The differences are found less than 0.2%. Therefore, the 46×62 grid size is used throughout the numerical calculations.

4. Results and discussion

4.1. Wall temperature rise

The wall temperature rises along the longitudinal direction, $T_1 - T_{in}, T_2 - T_{in}, T_3 - T_{in}$, are shown vs. the cell Reynolds number Re in Fig. 4 for the air experiment and in Fig. 5 for the water experiment. It is seen that as the value of Re increases, the temperature rise changes from 8.7°C to 57.6°C for air flow and 4.0°C to 23.7°C for water flow. It is also seen that the maximum differences among the temperature rises for T_1, T_2 and T_3 take place at the lowest Re and are within 5°C for both experiments, indicating that a good uniformity in the wall temperature is achieved for the present heat sink. For the comparison purpose, we show in Fig. 4 the wall temperature rises under the same power input for air cooling a sintered bronze-bead system with a particle diameter $d_p = 1.59$ mm and a size 5 cm × 5 cm × 1 cm [11]. The wall temperatures T_1, T_2 and T_3 in that case are taken at the corresponding wall locations and interp-

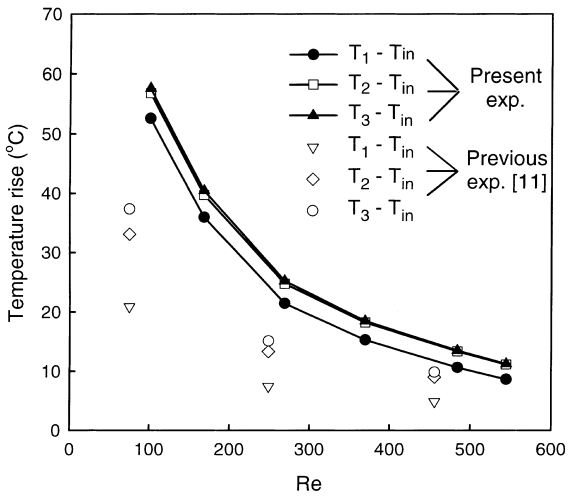

Fig. 4. Air experiment: the plot of the wall temperature rise vs. Re at $Q_t = 20$ W, with T_1, T_2 and T_3 denoting the wall temperatures at locations $L/6$, $L/2$ and $5L/6$ from the inlet of the heat sink, respectively. The wall temperature rises in Ref. [11] are shown for comparison.

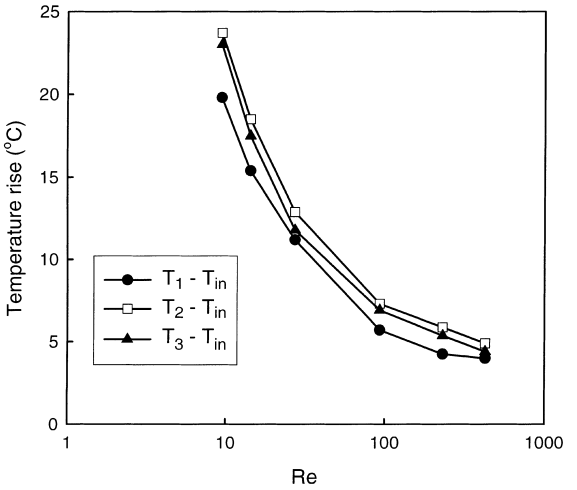

Fig. 5. Water experiment: the plot of the wall temperature rise vs. *Re* at $Q_t = 106$ W.

olated from the temperature measurements therein. It is seen that there are significantly larger temperature variations in the wall temperature for the sintered bronze-bead system, although the mean wall temperature rises are lower than the present model due to the lower heat flux therein. Hence the present heat sink is preferred in eliminating the excess local high temperature of a heated wall.

4.2. Temperature fields

From the measured three-point wall temperature, we can obtain the fitted wall temperature profile $\theta_w(x)$ and, with the aforementioned theoretical analysis, calculate the detailed temperature fields for the solid matrix and the fluid, respectively. The calculated temperature profiles for air experiment is shown in Fig. 6 with $Re = 336$ ($G = 50$ l/min). Although in the tests the working fluid bulk was separated by unconnected ducts and discontinuous in space, the modeled fluid temperature profile is continuous, representing the volume averaged fluid temperature at the system level. It is seen that the temperature profiles for the fluid and the solid are significantly different. The dimensionless fluid temperature θ_f increases gradually along the x direction, while θ_s is askew distributed, indicating that a two-equation modeling is imperative.

The temperature profiles for the water experiment at $Re = 67.2$ ($G = 8.95$ ml/s) is shown in Fig. 7. The calculated dimensionless solid and fluid temperature profiles are displayed in Fig. 7(b) and (c), respectively, and the discrepancy between θ_f and θ_s, like air flow, is obvious. In the water flow case, however, the solid temperature variations in both the transverse and longitudinal directions are more pronounced due to the lower value

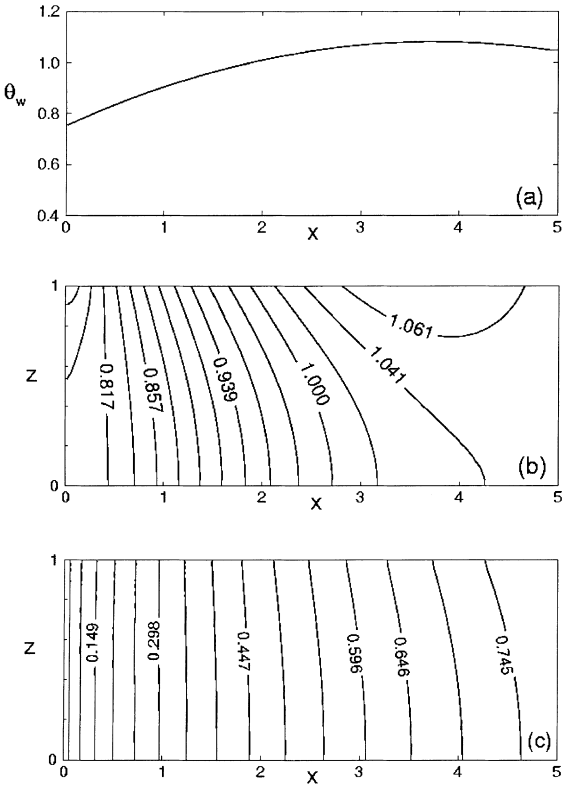

Fig. 6. Calculated temperature fields for air flow: (a) the fitted wall temperature profile $\theta_w(x)$; (b) the solid temperature θ_s; (c) the fluid temperature θ_f.

of κ. Accordingly, the fluid temperature profile is more askew distributed than the air flow case.

The Nusselt numbers for the two fluids are also calculated and compared to those with the results calculated under the isothermal boundary condition (14). The discrepancies are found less than 3%. For the sake of convenience, the following theoretical results are presented based on the isothermal boundary condition instead of the measured wall temperature profiles.

4.3. Nusselt number

In this subsection, we present both measured and calculated results for the Nusselt numbers based on the wall to the inlet fluid temperature difference. The functional dependence of the measured Nusselt numbers on the Reynolds number *Re* is shown in Fig. 8 for air flow and Fig. 9 for water flow, respectively, along with the calculated results from the theoretical analysis. For the air experiment, the experimental data is fitted by the following power functional correlation

$$Nu = 0.544 Re^{1.05}. \tag{16}$$

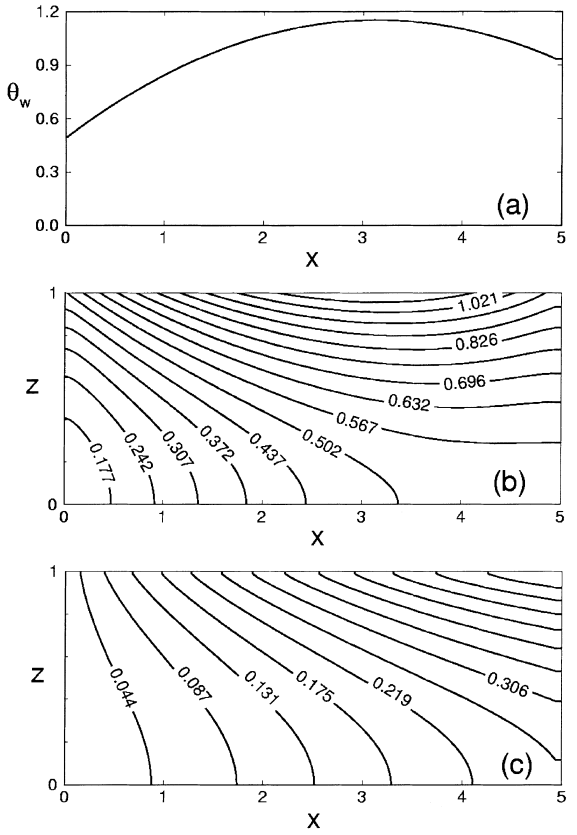

Fig. 7. Calculated temperature fields for water flow: (a) the fitted wall temperature profile $\theta_w(x)$; (b) the solid temperature θ_s; (c) the fluid temperature θ_f.

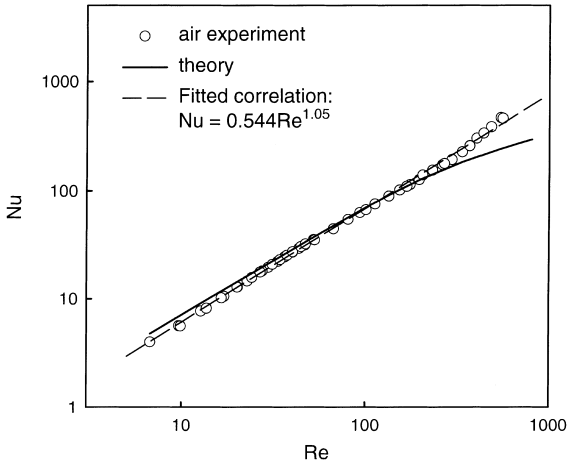

Fig. 8. Nusselt number for air flow: experimental results and comparison with theoretical analysis.

The maximum deviation of this correlation from the experimental data is 14%. The fitted curve has been shown in Fig. 8. The comparison between the experimental data and the theoretical results shows that over most of the *Re* range, the agreement is satisfactory. At $Re = 350$, the experimental results exceed the theoretical values by 20% or more as *Re* further increases. The higher experimental values may be due to the transition to turbulence occurring in the upstream flow channel, where the diameter was larger and the channel Reynolds number would exceed the transition Reynolds number, typically 2300 for in-channel flow.

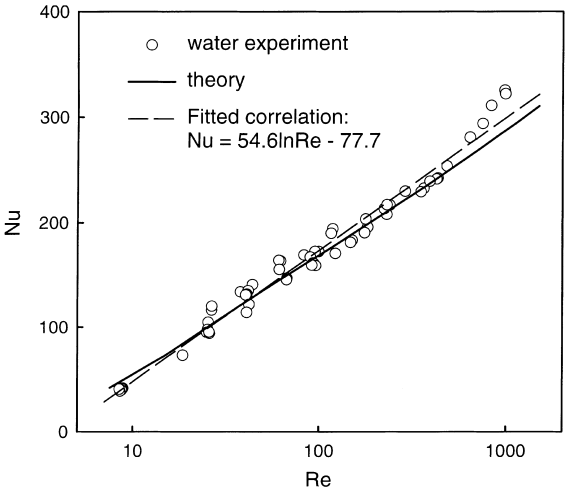

Fig. 9. Nusselt number for water flow: experimental results and comparison with theoretical analysis.

For the water experiment, we obtain the fitted *Re–Nu* correlation as

$$Nu = 54.6 \ln Re - 77.7, \tag{17}$$

which is plotted in Fig. 9 against the experimental data. A maximum deviation of 16% is found for this correlation compared with the experimental data. Again we compare the theory and the experiment and the find that they are fairly close at the test range of *Re*. The higher experimental values of *Nu* at a large value of *Re* can be explained in the same way as the air experiment.

It has been seen that in the similar range of the Reynolds number, the power dependence of *Re* found for the air experiment is stronger than the logarithmic dependence for the water experiment, as shown in the fitted Eqs. (16) and (17). This difference can be attributed to the significantly different values in the solid–fluid thermal conductivity ratio κ for the two cases. In the air experiment, the value of κ is one order-of-magnitude higher and the heat conduction inside the solid is stronger. Thus the overall thermal resistance arises mainly from the air side and a convection-dominated dependence (Re^n dependence) is achievable. For the water experiment, κ is lower, the heat conduction in the solid becomes comparable in magnitude to the convective transport of the fluid and thus the overall heat

transfer is conjointly determined by both heat transfer mechanisms, suggesting a less strong dependence on the flow parameter *Re*.

It is noted that the heat transfer coefficient *h*, which is of practical interests, ranged from 7.6×10^{-4} to 0.106 W/cm^2 °C for the air flow case and from 0.21 to 1.64 W/cm^2 °C for the water flow case. The results for the water experiment are much less than the heat transfer coefficients for microchannels, in which a heat flux 790 W/cm^2 was attained with a maximum wall rise to inlet water temperature of 71°C [1]. If we could reduce the unit cell dimension for the present heat sink to that of the microchannel, which is 100 μm [1], the values of h for water flow would range from 5.0–39.4 W/cm^2 °C. This conceptual comparison suggests that the present heat sink essentially could compete with the microchannels. However, due to the limitation in the scope of this study, in what follows we will present a detailed comparison of the straight-duct characterized porous systems with bead-characterized counterparts instead of the microchannel structure.

4.4. Heat transfer comparison with bead-characterized systems

The present experimental results for *Nu* are compared with the results from two reported cases: a sintered bronze-bead system with $d_p = 1.59$ mm in Hwang et al's work [11] and a packed-bead system with $d_p = 8$ mm from [7]. In the first case, air was used as the working fluid and the wall temperature profiles were presented there, but the overall heat transfer results were not given. Here *Nu* is calculated in the form of Eq. (4) for the bead system to make the comparison. For consistency, in the calculation of *Nu*, the arithmetic average of T_1, T_2 and T_3 are used as the mean wall temperature $T_{w,m}$. Such a procedure leads to a deviation generally within 3% in the spatial-weighted average wall temperature from their more detailed measurements, which is negligible in the present analysis. The results for *Nu* are displayed in Fig. 10, together with the present correlation Eq. (16) for air flow. It is found that Hwang et al's results are overall slightly higher than those from Eq. (16). Considering that the ratio $A_l = 6.29$ in their work was higher than $A_l = 5$ in the present case, which could contribute to the surplus in *Nu*, the heat transfer results from the two systems are essentially very close. In the second case [7], water was used as the working fluid and the Nusselt number was based on the effective conductivity and channel length. The Nusselt number is recalculated in terms of the fluid conductivity and height, i.e., Eq. (4), and displayed in Fig. 10 in comparison with the present correlation (17) for the water experiment. It is seen that our results are overall twice of those for the packed bead system.

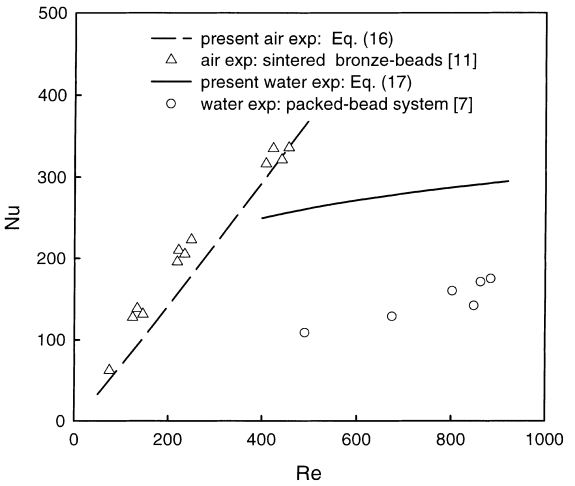

Fig. 10. Heat transfer comparison of the present heat sinks with the bead-characterized systems from [11] and [7].

With the theoretical modeling given in this paper, we may further compare the heat transfer performance of the present straight-duct characterized heat sinks with the sintered copper-bead systems investigated by Peterson and Chang [12]. The heat dissipation capacity of Peterson and Chang's systems was high among the reported results for the similar systems. In their work, the heat transfer coefficients were presented for six tests with three particle sizes and two inlet water temperatures and the system parameters are listed in Table 1. Since our

Table 1
Comparison of the straight-duct-characterized heat sinks with the sintered copper-bead heat sinks tested by Peterson and Chang [12]

No.	Parameters				Nusselt numbers		
	l (mm)	T_{in} (°C)	$Re\,Pr$	Flow resistance ratio τ_1/τ_2	Ref. [12]	Present heat sink	Present heat sinks under $\tau_1/\tau_2 = 1$
1	0.97	60	27.2	10.4	130	136	560
2	0.97	30	29.2	10.4	128	145	585
3	0.54	60	15.0	14.6	146	140	776
4	0.54	30	16.0	14.6	130	150	816
5	0.39	60	39.1	9.23	59.7	53.5	313
6	0.39	30	41.9	9.23	53.5	57.1	327

test model is different from their test systems, such as in the length scale of the unit cell and the material of the solid matrix, we theoretically calculate the corresponding Nusselt numbers for the present heat sinks based on their reported parameters [12] except the geometry of the unit cell. The calculated results for the present heat sinks are listed in the seventh column of Table 1, in comparison with the Nusselt numbers for the sintered bead systems in the sixth column of Table 1, which are evaluated with the heat transfer coefficients from their systems. It is shown that these two columns of results are very close despite of the different unit-cell geometries characteristic in the two types of systems. This conclusion seems to be debatable at first glance since for the sintered bead system, the flow is more tortuous, a higher value of H_{uc} is achievable and thus a higher level of heat transfer is expected. This doubt can be cleared up by considering the fact that during the sintering process, the neck growth between beads takes place very randomly and, unavoidably, results in nonuniform or even poor consolidation in space [20], which undermines the heat conduction in the solid matrix and thus offsets the gain in Nu due to the increase in H_{uc}. It should be pointed out that in most thermal energy storage processes where the transverse conduction is insignificant, it is the bead-characterized instead of the straight structure that provides more effective heat transfer and is widely used in practice [21,22].

It is of practical concern to take into account the flow resistance in the heat transfer analysis. The unit-cell-level flow resistance of the heat sink characterized by straight circular ducts can be estimated by the following equation

$$\tau_1 = \frac{2\left(c_{\mathrm{fapp}} Re_{\mathrm{c}}\right)\mu u_{\mathrm{m}}}{\varepsilon d_{\mathrm{c}}^2}. \tag{18}$$

Here Re_c is the Reynolds number based on d_c and c_{fapp} is the apparent average friction coefficient for a laminar flow in a circular tube, which accounts for the hydraulic entrance effect. The determination of the product $(c_{fapp}Re_c)$ can be found in [18]. For the sintered bead systems, the following formula is used to evaluate the flow resistance [12]

$$\tau_2 = \mu \frac{u_{\mathrm{m}}}{\gamma}, \tag{19}$$

where the permeability γ for the sintered systems was given in [12]. The results for the flow resistance ratio τ_2/τ_1 have been shown in the fifth column of Table 1 for all the six tests. It is seen that the flow resistance ratios vary from 9.23 to 14.6, indicating that the flow resistance for a straight-duct-characterized heat sink is greatly reduced owing to the straightness in microstructure. On the other hand, if Re for the present heat sink is increased so that the flow resistance reaches at the same level as the sintered bead systems, i.e., $\tau_2/\tau_1 = 1$, it is anticipated that a higher heat transfer ability can be achieved in comparison with the bead-characterized counterparts. As such, the Nusselt numbers are calculated for the straight-duct characterized heat sinks under the same flow resistance as the corresponding sintered bead systems. The results, as listed in the eighth column of Table 1, are about 4–6 times of the Nusselt numbers from the sintered bead systems.

5. Conclusions

In this paper, the heat transfer measurements and theoretical analysis for a straight-duct characterized porous heat sink were performed for both air and water flows. The experiments were conducted with the cell Reynolds number Re ranging from 6.7 to 545 for air flow and 8.5 to 990 for water flow. The wall temperatures and the Nusselt numbers are presented and the functional dependence of Nu on Re is correlated for both flows, as shown in Eqs. (16) and (17) and Figs. 8 and 9. In the theoretical analysis, the detailed temperature fields in the heat sink are calculated and presented. Comparison of the theoretical results with the experimental measurements is conducted and satisfactory agreement is achieved. Furthermore, the comparison with the reported results from bead-characterized porous systems shows that the straight-duct-characterized heat sink provides a more competitive heat transfer capacity when the flow resistance parameter is taken into account, and is of practical advantage in the designing of miniaturized heat sinks.

References

[1] D.B. Tuckerman, R.F.W. Pease, High-performance heat sinking for VLSI, IEEE Electron Device Lett. 2 (1981) 126–129.
[2] D.B. Tuckerman, R.F.W. Pease, Ultrahigh thermal conductance microstructures for integrated circuits, IEEE Proc. 32nd Electronics Conference, 1982, pp. 145–149.
[3] X. Yin, H.H. Bau, Uniform channel micro heat exchangers, J. Electron. Packag. 119 (1997) 89–94.
[4] T.M. Kuzay, Cryogenic cooling of X-ray crystals using a porous matrix, Rev. Sci. Instrum 63 (1992) 468–472.
[5] M.L. Hunt, C.L. Tien, Effects of thermal dispersion on forced convection in fibrous media, Int. J. Heat Mass Transfer 31 (1988) 301–309.
[6] F.C. Chou, W.Y. Lien, S.H. Lin, Analysis and experiment of non-Darcian convection in horizontal square packed-sphere channels–I. Forced convection, Int. J. Heat Mass Transfer 35 (1992) 195–205.
[7] K. Vafai, R.L. Alkire, C.L. Tien, An experimental investigation of heat transfer in variable porosity media, J. Heat Transfer 107 (1985) 642–647.

[8] P. Cheng, C.T. Hsu, A. Chowdhury, Forced convection in the entrance region of a packed channel with asymmetric heating, J. Heat Transfer 110 (1988) 946–954.
[9] A. Amiri, K. Vafai, Analysis of dispersion effects and non-thermal equilibrium, non-Darcian, variable porosity incompressible flow through porous media, Int. J. Heat Mass Transfer 37 (1994) 939–954.
[10] G.J. Hwang, C.H. Chao, Heat transfer measurement and analysis for sintered porous channels, J. Heat Transfer 116 (1994) 456–464.
[11] G.J. Hwang, C.C. Wu, C.H. Chao, Investigation of non-Darcian forced convection in an asymmetrically heated sintered porous channel, J. Heat Transfer 117 (1995) 725–732.
[12] G.P. Peterson, C.S. Chang, Two-phase heat dissipation utilizing porous-channels of high-conductivity material, J. Heat Transfer 120 (1998) 243–252.
[13] R.G. Carbonell, S. Whitaker, Heat and mass transfer in porous media, in: J. Bear, M.Y. Corapcioglu (Eds.), Fundamentals of Transport Phenomena in Porous Media, Martinus Nijhoff, Dordrecht, The Netherlands, 1984, pp. 123–198.
[14] M. Quintard, S. Whitaker, One and two-equation models for transient diffusion processes in two-phase systems, Adv. Heat Transfer, vol. 23, Academic Press, New York, 1993, pp. 369–465.
[15] H.Y. Zhang, X.Y. Huang, C.Y. Liu, Studies of convection heat transfer in porous media characterized by straight ducts, in: Proceedings of the Fifth ASME/JSME Thermal Engineering Joint Conference, 1999.
[16] H.Y. Zhang, X.Y. Huang, Volumetric heat transfer coefficients in solid–fluid porous media: closure problem, thermal analysis and model improvement with fluid flow, Int. J. Heat Mass Transfer 43 (2000) 3417–3432.
[17] R.J. Moffat, Describing the uncertainties in experimental results, Exp. Thermal Fluid Sci. 1 (1988) 3–17.
[18] W.M. Kays, M.E.C. Crawford, Convective Heat and Mass Transfer, third ed., McGraw-Hill, New York, 1993.
[19] S.V. Patankar, Numerical Heat Transfer and Fluid Flow, Hemisphere, New York, 1980.
[20] R.M. German, Sintering Theory and Practice, Wiley, New York, 1996 (Chapter 4).
[21] K.A.R. Ismail, R. Stuginsky Jr., A parametric study on possible fixed bed models for pcm and sensible heat storage, Appl. Thermal Eng. 19 (1999) 757–788.
[22] C.C. Wu, G.J. Hwang, Flow and heat transfer characteristics inside packed and fluidized beds, J. Heat Transfer 120 (1998) 667–673.